Monthly Notices of the ROYAL ASTRONOMICAL SOCIETY

MNRAS **543,** 1935–1944 (2025) https://doi.org/10.1093/mnras/staf1498
Advance Access publication 2025 September 11

Radio emission from a nearby M dwarf binary

Kelvin Wandia [1]★ Michael A. Garrett,[1,2] Robert J. Beswick,[1] Jack F. Radcliffe [1,3] Vishal Gajjar,[4,5] David Williams-Baldwin [1] Chenoa Tremblay [4,6] Iain McDonald [1] Alex Andersson [7] and Andrew Siemion[1,4,5,7,8,9,10]

[1]*Jodrell Bank Centre for Astrophysics (JBCA), Department of Physics & Astronomy, Alan Turing Building, The University of Manchester, Manchester, M13 9PL, UK*
[2]*Leiden Observatory, Leiden University, PO Box 9513, NL-2300 RA Leiden, the Netherlands*
[3]*Department of Physics, University of Pretoria, Lynnwood Road, Hatfield, Pretoria 0083, South Africa*
[4]*SETI Institute, 339 Bernardo Ave, Suite 200, Mountain View, CA 94043, USA*
[5]*Berkeley SETI Research Center, University of California, Berkeley, CA 94720, USA*
[6]*Astrophysics, Department of Physics, University of Oxford, Keble Road, Oxford OX1 3RH, UK*
[7]*Berkeley SETI Research Center, University of California, Berkeley, CA 94720, USA*
[8]*Institute of Space Sciences and Astronomy, University of Malta, Msida MSD2080, Malta*
[9]*Department of Physics and Astronomy, University of New Mexico, Albuquerque, NM 87131, USA*
[10]*Breakthrough Listen, Astrophysics, Department of Physics, The University of Oxford, Keble Road, Oxford OX1 3RH, UK*

Accepted 2025 September 2. Received 2025 September 2; in original form 2025 April 26

ABSTRACT

We present the detection of the binary system 2MASS J02132062+3648506 AB using the Karl G. Jansky Very Large Array archive data observed at 4–8 GHz. The system is a triple consisting of a tight binary (∼0.2 arcsec) of two M dwarfs of spectral types M4.5 and M6.5 and a wide T3 brown dwarf companion (∼16.4 arcsec). The binary displays coronal and chromospheric activity as traced by previously measured X-ray flux and H α emission. We detect the unresolved binary at a peak flux density of ∼356 μJybeam^{-1} at a signal-to-noise ratio (SNR) of ∼36 and determine a radio luminosity of $\log L_{\rm R}/\log L_{\rm bol} \sim -7.76$. The radio emission is quiescent, polarized at a mean circular polarization fraction $f_{\rm c} = 45.20 \pm 1.58\%$ and exhibits a spectral index $\alpha = -0.44 \pm 0.07$. We probe the binary using the Enhanced Multi-Element Remotely Linked Interferometer Network (e-MERLIN) with an angular resolution of ∼40 mas at 5 GHz and detect a component at a peak flux density of ∼90 μJy beam^{-1} at a SNR ∼ 5. We propose a gyrosynchrotron origin for the radio emission and estimate a magnetic field strength $B < 174.86$ G, an emitting region of size $L < 1.54$ times the radius of the M4.5 primary and a plasma number density $n_{\rm e} < 2.91 \times 10^5$ cm^{-3}. The brown dwarf companion is not detected. Additionally, we have analysed observations of 2MASS J04183483+213127, a chromospherically active L5 brown dwarf which is also not detected and can only place 3σ flux density upper limits at 36.9 μJy beam^{-1} and 42.3 μJy beam^{-1} for Stokes I and V, respectively.

Key words: stars: activity – stars: low mass – stars: magnetic fields.

1 INTRODUCTION

Low-mass main-sequence stars of spectral class M (dwarfs) dominate the stellar content of the Milky Way and constitute 70–75 per cent of the total stellar population (e.g. Henry et al. 2006; Winters et al. 2019). Volume-limited surveys for M dwarfs reveal stellar multiplicity and companion rates of ∼26.8% and 32.4%, respectively (see Winters et al. 2019). As stars transit through the M class, their mass and radius decrease, resulting in physical changes to the stars. Besides the directly observable changes e.g. the luminosity, the stellar interior also undergoes a transformation. At a mass $M > 0.35\,{\rm M}_\odot$, the interior is Solar-like and consists of the core and a radiative and convective zone separated by a tachocline. For stars of lower mass, the radiative zone disappears, resulting in a fully convective interior (see Baraffe & Chabrier 2018). This decrease in mass results in a decrease in pressure on the core and subsequently a decrease in temperature. At a mass ∼0.075 $\rm M_\odot$ (78.5 $M_{\rm Jup}$) (Chabrier et al. 2023) the core temperature is less than the critical temperature of $T > 3 \times 10^6$ K (Nelson, Rappaport & Chiang 1993; Burrows et al. 1997) required to start and sustain hydrogen fusion and the hydrogen mass burning limit is reached. We note that metallicity plays an important role in the hydrogen mass burning limit.

Although the existence of very low-mass stars and brown dwarfs was theorised in the 1960s (Kumar 1962), they remained elusive to observational campaigns. Until the mid 1990s, the coolest confirmed main-sequence stars were of spectral type M9.5 V leading to the view that the main sequence ended there. This idea was revised after the discovery of sub-stellar objects by Kirkpatrick et al. (1999) using the 2-Micron All-Sky Survey (2MASS; Skrutskie et al. 2006). The

★ E-mail: kelvin.wandia@manchester.ac.uk

effective temperatures of these objects did not align with the original stellar classification, and they were assigned the spectral class L and T. Most of the objects in the new classes, along with some late-type M dwarfs, are brown dwarfs. Objects of spectral types ≥M7 V are commonly refered to as ultracool dwarfs (Cushing 2006). We note that brown dwarfs are physically defined by mass rather than the effective temperatures (Reiners et al. 2007) . A common method to assess the substellarity of young brown dwarfs is the so-called Lithium test. This test is based on the premise of efficient mixing in the object's convective layers and the core never reaching the ignition temperature of Lithium at 2.5×10^6 K, which is lower than that of hydrogen. Consequently, any detection of the Lithium 1 resonance feature at 6708 Å indicates the object is unable to fuse hydrogen (e.g. Basri, Marcy & Graham 1996; Rebolo et al. 1996) and is potentially substellar.

Chromospheric and coronal activity is routinely observed in many stars. Common tracers of activity in low-mass stars are the first hydrogen Balmer line, Hα, emitted at optical wavelengths from chromospheric gas heated to $\sim 10^4$ K and X-ray fluxes produced by plasma heated to $\sim 10^6$ K in the corona. This activity is driven by magnetic fields believed to be generated by powerful dynamos at work in the stars. For Solar-like stars with a radiative core and a convective envelope, an $\alpha\Omega$ dynamo (Parker 1955) is at work whilst for fully convective stars, an α^2 dynamo has been proposed. Although the exact dynamo mechanism is still under investigation, Chabrier & Küker (2006), Dobler, Stix & Brandenburg (2006), and Browning (2008) have shown that the α^2 dynamo is able to generate and sustain large-scale magnetic fields.

A critical component of dynamo theory is rotation, which presents an interesting interplay with activity. Activity is observed to increase with rotation for stars ranging from mid-F spectral types to M8 (see Mohanty et al. 2002) and peaks in L0 dwarfs with ∼90% of objects in this spectral type showing activity, then decreases to 50% for L5 dwarfs and becomes increasingly rare in later type objects (Schmidt et al. 2015). The relationship between the rotation and activity has led to the formulation of the rotation-activity paradigm (see Reiners 2012). Although activity increases with rotation it is ultimately constrained by the saturation limit. The saturation limit is the ratio of the corresponding X-ray luminosity L_X or the Hα luminosity $L_{H\alpha}$ to the bolometric luminosity and is approximately $\log L_X/\log L_{bol} \approx -3$ (see Vilhu 1984) and $\log L_{H\alpha}/\log L_{bol} \approx -3.8$ for most M dwarfs. Indeed, Newton et al. (2017) have demonstrated that rapid rotators have $L_{H\alpha}/L_{bol}$ close to the saturation limit. In regards to binaries, tidal interactions and the exchange of angular momentum increases the rotation in close binaries (<7 arcsec) and, in turn, the chromospheric emission (Hawley, Gizis & Reid 1996; Morgan et al. 2012).

Particle acceleration mechanisms mediated by magnetic fields lead to coherent and incoherent emissions at radio frequencies. Incoherent emission is produced through several radiation mechanisms: thermal bremsstrahlung generated by free electrons in the heated bulk plasma, gyroemission arising from thermal electrons, and gyrosynchrotron originating from non-thermal electrons accelerated along magnetic field lines to mildly relativistic velocities (see Nindos 2020, and references therein). Coherent emission is primarily from plasma emission (see Melrose 1980) and the electron cyclotron maser (see Wu & Lee 1979; Melrose & Dulk 1982; Melrose 2017). Following the rotation–activity relationship, a radio activity–rotation relationship ensues. Under this paradigm radio emission from stars of spectral type M0–M6 with rotational velocities >5 km s^{-1} increases with rotation and saturates at a ratio of the corresponding radio luminosity L_R to the bolometric luminosity at $\log L_R/\log L_{bol} \approx 10^{-7.5}$and for later spectral types, $\log L_R/\log L_{bol}$ is independent of rotation (McLean et al. 2012). A partially analogous relationship is the Güdel–Benz relationship between soft X-ray and radio luminosity at 5 GHz given as $\log L_X \lesssim \log L_R + 15.5$ (Guedel & Benz 1993). This relationship is valid for all active stars but fails to explain the radio emission observed from ultra cool dwarfs (see Berger 2002). This is conceivably a consequence of saturation in X-ray emission and an unimpeded increase in the radio emission for rapidly rotating ultra cool dwarfs. We note in passing that rapid rotation is not the sole condition required for radio emission as demonstrated by the null detection of rapidly rotating low-mass stars by Antonova et al. (2013).

Motivated by the need to better understand the nature of the radio emission from ultracool dwarfs, we undertook an analysis of archival National Science Foundation Karl G. Jansky Very Large Array (VLA) data sets targeting the then recently discovered UCDs 2MASS J02132062+3648506 C of spectral type T3 and 2MASS J04183483+2131275 of spectral type L5. The T3 UCD is the tertiary component in an orbit around an X-ray active binary M dwarf and the L5 UCD is chromospherically active and a member of the Hyades cluster. Our aim was to characterize the radio properties and assess the implications of non-thermal emission mechanisms from the UCDs and the binary. In the sections that follow, we describe the targets and their relevant background in Section 2. Section 3 outlines the observational set-up and data analysis procedures. We present our results and interpretation in Section 4 and conclude with a summary of our findings and their significance in Section 5.

2 TARGETS

2.1 2MASS J0213+3648 ABC

The M dwarf binary 2MASS J02132062+3648506 AB (hereinafter 2M0213 AB) was first detected by Riaz, Gizis & Harvin (2006) and reported as a single star of spectral type M4.5. The star displayed significant X-ray emission at $\log(L_X/L_{bol}) = -3.16$ close to the saturation limit of −3. Further follow-up by Janson et al. (2012) characterized the star as a tight binary consisting of a primary and a secondary of spectral types M4.5 and M6.5 respectively and separated by ∼0.217 arcsec (Janson et al. 2014). The binary displays chromospheric activity as revealed by the wide equivalent widths of the Hα emission line at at 6.6–8.1 Å (Riaz et al. 2006; Deacon et al. 2017) and a Hα to bolometric luminosity ratio of $\log(L_{H\alpha}/L_{bol}) = -3.4$ (Deacon et al. 2017) which exceeds values typical for M dwarfs at $\log(L_{H\alpha}/L_{bol}) = -3.8$ (Czesla, Schneider & Schmitt 2008). Deacon et al. (2017) demonstrated that it is not physically possible for all the Hα emission to be emitted by the M6.5 dwarf, indicating the M4.5 primary is also chromospherically active. We emphasise that similar statements were not made for X-ray fluxes. 2M0213 AB is a rapid rotator, as demonstrated by the large projected rotational velocity $v \sin i \sim 25.1$ (Bowler et al. 2023). Considering the two components of 2M0213 AB are of spectral types M4.5 and M6.5, they are fully convective (Stassun et al. 2011) and are expected to have efficient dynamos capable of generating kilo-gauss magnetic fields (see Reiners 2012). The binary has a wide (∼16.4 arcsec, ∼234 au) brown dwarf companion of stellar type T3. Evolutionary models have placed the mass and effective temperature at 68 ± 7 M_{Jup} and 1641 ± 167 K, respectively (Deacon et al. 2017). The system is at a distance of 14.28 pc from the Sun (Lindegren et al.2021). See Table 1 for the properties of the system.

Table 1. Physical parameters of the 2MASS J0213+3648 ABC system and 2MASS J0418+2131. We highlight the discrepancy between the effective temperature $T_{\rm eff}$ and mass of the L5 and T3 object. $T_{\rm eff}$ and mass seem to increase as one progresses to a later spectral type. It is essential to recognise that these parameters are derived from different stellar evolutionary models, which are sensitive to initial conditions and have slightly different input physics.

Property	2MASS J0213+3648 ABC			2MASS J0418+2131
	2MASS J0213+3648 A	2MASS J0213+3648 B	2MASS J0213+3648 C	
Spectral type	M4.5[a]	M6.5[a]	T3[f]	L5[i]
Position	02h13m20.6754 + 36d48m51.5425[b]		02h13m19.8876 + 36d48m38.3116[k]	04h18m34.9970s + 21d31m26.63754s [l]
μ_α (mas yr^{-1})	31.1 ± 3.6[k]			141.2 ± 4.3[j]
μ_δ (mas yr^{-1})	50.1 ± 3.7[k]			-51.8 ± 4.0[j]
$\bar{\omega}$ (mas)	70.02 ± 0.20[b, d]			25.8 ± 2.9[j]
Epoch	2015.5		2014.12.14[k]	2015.4[l]
Separation	0.217 arcsec[c]		16.4 arcsec	
Mass	$0.26 \pm 0.06\,M_\odot$[c]	$0.09 \pm 0.03\,M_\odot$[c]	$68 \pm 7\,M_{\rm Jup}$[f]	$<60\,M_{\rm Jup}$[h]
$\log_{10}(L_{\rm X}/L_{\rm bol})$	-3.16[e]			
$v \sin i$ (km s^{-1})	25.1[g]			
$T_{\rm eff}$			1641 ± 167[f]	1581 ± 113[h]
$\log_{10}(L_{\rm H\alpha}/L_{\rm bol})$	-3.4[f]			-6.0[i]

[a]Janson et al. (2012).
[b]Lindegren et al. (2021b).
[c]Janson et al. (2014).
[d]Golovin et al. (2023).
[e]Riaz et al. (2006).
[f]Deacon et al. (2017).
[g]Bowler et al. (2023).
[h]Lodieu, Rebolo & Pérez-Garrido (2018).
[i]Pérez-Garrido, Lodieu & Rebolo (2017).
[j]Lodieu et al. (2019).
[k]Best et al. (2020).
[l]Marocco et al. (2021).

2.2 2MASS J0418+2131

2MASS J04183483+2131275 (hereinafter 2M0418) is a brown dwarf of spectral type L5 first reported by Pérez-Garrido et al. (2017). The brown dwarf is a member of the Hyades open cluster, the closest cluster to the Sun and has an age of 500–700 Myr (Pérez-Garrido et al. 2017) and is at a distance of 40.6 ± 2.7 pc. The L5 brown dwarf displays chromospheric activity as revealed by persistent Hα emission (Lodieu et al. 2018) at $\log_{10}L_{\rm H\alpha}/\log_{10}L_{\rm bol} \sim -6.0$ (Pérez-Garrido et al. 2017). Spectroscopic follow-up by Lodieu et al. (2018) has led to the detection of a Lithium feature at 6708 Å, confirming the sub-stellarity of the object and placing mass upper limits at $<60\,M_{\rm Jup}$ (Lodieu et al. 2018). The properties of the brown dwarf are listed in Table 1.

3 METHODS

3.1 VLA observations

We have used unpublished (to the best of our knowledge) archival VLA observations (PI: Jan Forbrich) conducted on 2017-11-15 in response to the detection of a nearby T3 brown dwarf companion to 2M0213 AB by Deacon et al. (2017). Observations were also conducted for 2M0418, a chromospherically active L5 brown dwarf detected by Pérez-Garrido et al. (2017). The observations utilized the B configuration of the VLA at C band (4–8 GHz). The observing bandwidth was divided into 32 spectral windows (spws). The standard VLA calibrator 3C286 was observed for flux and bandpass calibration and J0204+3649 was observed as an amplitude and phase calibrator. The pointing centre was based on the position of 2M0213 AB at coordinates reported by Janson et al. (2012). The coordinates are at epoch 2007-06-01. Similarly, the pointing centre for 2M0418 was based on coordinates reported in the original 2MASS catalogue (see Cutri et al. 2003). The proper motion of the two targets was not considered. The full details of the proper motion effects on the astrometry at the VLA epoch of observation are discussed in Section 4.1. The targets were observed over twelve scans each ∼4 min and 36 s long, yielding a total on-target time of ∼55 min. The data were recorded in full polarization mode.

3.2 e-MERLIN observations

Follow-up observations of the 2M0213 AB were conducted using the seven-element (six telescopes are often used for regular observations) Electronic Multi Element Remotely Linked Interferometer Network (e-MERLIN; Garrington et al. 2004) at C band (4.82–5.33 GHz) using five antennas over a 24-h period from 2025-02-24 to 2025-02-25. Three calibrators were observed (PI Wandia): a flux calibrator 3C286 (1331+3030), a bandpass calibrator OQ208 (1407+2827), which is also useful for polarization leakage calibration and the phase calibrator 0213+3652 located $\sim 0.11^\circ$ from the target. During the observations, one antenna failed, resulting in a five-telescope experiment. The data were also heavily flagged due to radio interference leading to noise levels far beyond the expected limits of a six-antenna interference-free data. Consequently, re-observations using the same observation set-up were requested and conducted intermittently using six telescopes over a 48-hour period from 2025-03-13 to 2025-03-14. The target was observed over 173 scans at a median scan duration of ∼5 min and 56 s, yielding a total on-target time of ∼17.1 h. The data were recorded at full polarization.

3.3 Data analysis

We have processed the VLA data using two different versions of the VLA pipeline, which is based on the Common Astronomy Software

Applications (CASA; CASA Team et al. 2022). We have used CASA 5.1.0–74, the recommended version and the recent version of the pipeline, which is based on CASA 6.6.1–17.[1]We found the results comparable and opted to use CASA 6.6.1–17. The pipeline exports the data from a Science Data Model-Binary Data Format [SDM-BDF]) file to a measurement set, performs Hanning smoothing, antenna position corrections, gain and amplitude calibration among other VLA specific calibration procedures. The data are also automatically flagged at various stages and the end products are science ready visibilities stored in a measurement set. A description of the CASA pipeline stages is found in Kent et al. (2020). We have made deconvolved images of the calibrated visibilities using the CASA task `tclean` to produce continuum images spanning the entire bandwidth using the multi-term multi-frequency deconvolver (Rau & Cornwell 2011), which is native to `tclean`, to account for the wide bandwidth. All images are Briggs weighted (Briggs 1995) with a robust parameter of 0.5.

To measure the spectral index, we split the bandwidth into eight chunks each 500 MHz in size and image them individually. We then mask out any emission above $5\sigma_{\rm t}$ where $\sigma_{\rm t}$ is the thermal noise in the image and constrain the emission about the known position using a rectangular box. For each of the images, the integrated flux and the error is then extracted by fitting an elliptical Gaussian using the CASA task `imfit`. Finally, we use bootstrapping to resample the fluxes and their associated errors and fit a line of best fit. The spectral index is then determined from the slope of the fitted line. To prepare the data for variability analysis, we first mask the target position, model the background sources within the primary beam and shift the pointing centre of the background subtracted visibilities to the proper motion corrected positions of the target using the CASA task `phaseshift`. Using the CASA toolkit `casatools`.[2] `table` and `ms` tools to parse the visibilities, we average all frequency channels, spectral windows, and baselines to obtain a single visibility per integration time for correlations `RR` and `LL`. We note that analysis in the visibility domain circumvents challenges associated with synthesis imaging and deconvolution e.g. imaging artefacts. The noise properties are also well characterized in the visibility domain making it easier to identify calibration and systematic errors. As a result, analysis in the visibility domain yields more reliable estimates. We follow a similar approach in processing the visibilities for the observation of 2M0418.

The e-MERLIN data were processed using the e-MERLIN CASA pipeline (Moldon 2018) based on CASA version 5.8.0.[3] The pipeline first imports the fits files to a measurement set. The data are then flagged to remove radio frequency interference, flux, bandpass and gain calibration are performed and the data are flagged again. The fully calibrated data are then split into individual fields and imaged using `tclean`. A similar weighting scheme and robust parameter as used for the VLA observations are applied.

4 RESULTS AND DISCUSSION

4.1 Astrometry

2M0213 AB is detected by *Gaia* and has been catalogued in the second (Gaia DR2; Gaia Collaboration 2018) and the third (Gaia DR3; Gaia Collaboration 2023) data releases (DR) but remains unresolved in the two catalogues. The wide T3 companion is below the detection threshold. To assess the quality of astrometry, we analyse four goodness of fit statistics: the `astrometric_excess_noise` (ϵ_i), `astrometric_excess_noise_sig` (D), `astrometric_params_solved`, and the `renormalised unit weight error` (`RUWE`). ϵ_i measures the noise introduced due to the discrepancy between the observed source's astrometry and *Gaia*'s astrometric model used for the fit. D is the significance of ϵ_i with $D > 2$ indicating significance (see Lindegren et al. 2012). We note that in Gaia DR2, ϵ_i is potentially inflated due to the inclusion of modelling errors. Significant values of ϵ_i have been proposed as a signature of unresolved binaries due to orbital wobbles of the components (see Ghandi et al. 2022). The `astrometric_params_solved` lists the astrometric parameters that have been solved for. A good astrometric solution typically returns the six main astrometric parameters (position in right ascension α and declination δ, associated proper motions in right ascension μ_α and declination μ_δ, the parallax $\bar{\omega}$ and the radial velocity $v_{\rm r}$). Finally, the `RUWE` indicates the deviation of the astrometric fit from the observed data (Lindegren et al. 2021b) and has been identified as a good indicator of stellar multiplicity (e.g. Belokurov et al. 2020; Castro-Ginard et al. 2024). A guiding heuristic for a reliable measurement is `RUWE` < 1.4. Larger values are broadly regarded as an indication of poor measurement and or binarity/multiplicity. Despite the chances that larger `RUWE` arises from poor measurements it enhances the understanding of an object, especially when combined with other goodness-of-fit parameters.

2M0213 AB has the following five astrometric parameters solved for and catalogued in Gaia DR2, α, δ, μ_α, μ_δ and $\bar{\omega}$. Gaia DR3 has only three catalogued parameters α, δ and $v_{\rm r}$. As a result, we opt to use the astrometric solutions of the former. The binary has $D \sim 145$, which notably indicates that ϵ_i is significant. As `RUWE` values are not estimated in the Gaia DR2 catalogue; we use `textscgaiadr2-ruwe-tools`.[4] to determine `RUWE` and obtain a value of $\sim$3. The large `RUWE` coupled with the significant ϵ_i is indicative of binarity. The poor astrometry, especially in Gaia DR3, could be interpreted in the context of a slightly resolved binary, leading to poor astrometric fitting by the *Gaia* pipeline. We however caution that the possibility of the measurement being unreliable cannot be completely dismissed. Further astrometry is obtained from a volume-limited survey of ultracool dwarfs within 25 pc using the United Kingdom Infra-Red Telescope/Wide Field Camera (UKIRT/WFCAM) by Best et al. (2020), which has targeted 2M0213 ABC and, in particular, the low-mass T3 component. The UKIRT/WFCAM parallaxes for 2M0213 AB are in agreement with those from Gaia DR2, while the measured proper motions of 2M0213 C at $\mu_\alpha \sim 31.1 \pm 3.6$ mas yr^{-1} and $\mu_\delta = 50.1 \pm 3.7$ mas yr^{-1} significantly differ from those of 2M0213 AB measured by *Gaia* at $\mu_\alpha = 65.38 \pm 0.46$ mas yr^{-1} and $\mu_\delta = 64.89 \pm 0.38$ mas yr^{-1}. Since the T3 brown dwarf is comoving with 2M0213 AB, the components in the system share the same proper motion. We note that the proper motions for 2M0213 ABC from Best et al. (2020), which we adopt for our analysis, are also in agreement with proper motions from Lépine & Gaidos (2011) at $\mu_\alpha = 24$ mas yr^{-1} and $\mu_\delta = 47$ mas yr^{-1}.

The pointing centre for the observations of 2M0213 ABC was based on coordinates from Janson et al. (2012) at epoch 2007-06-01. The scheduling did not account for the proper motion as the coordinates were not propagated to the VLA epoch of observation:

[1] https://science.nrao.edu/facilities/vla/data-processing/pipeline
[2] https://casadocs.readthedocs.io/en/stable/api/casatools.html
[3] https://github.com/e-merlin/eMERLIN_CASA_pipeline
[4] https://github.com/agabrown/gaiadr2-ruwe-tools/tree/master

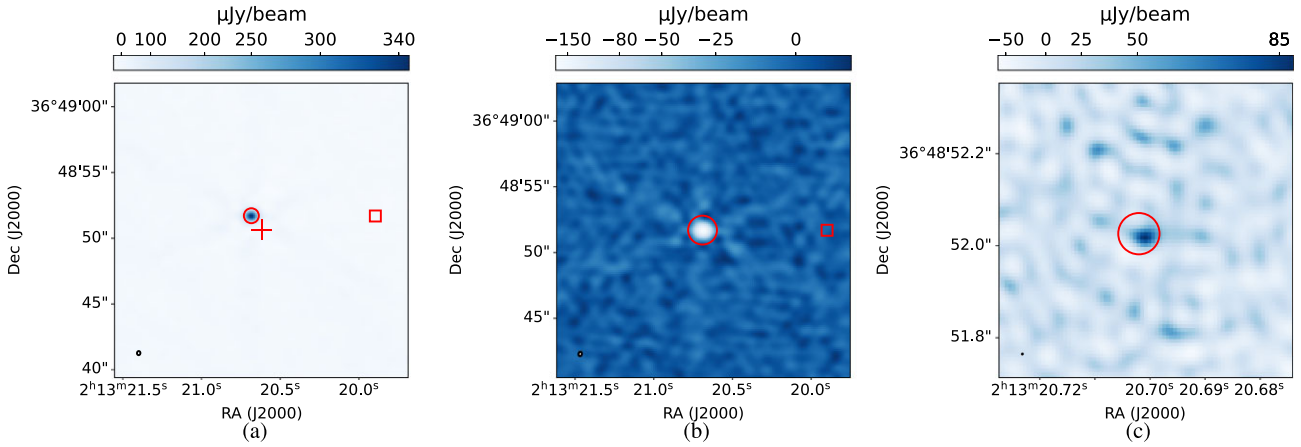

Figure 1. (a) Stokes I image of 2M0213 AB. The binary is unresolved and enclosed in the large circle . The binary is detected at a peak flux density of $\sim$356 μJy beam^{-1}. The 1σ r.m.s noise in the image is $\sim$10 μJy beam^{-1} giving a SNR $\sim$ 36. The binary at the true coordinates at epoch 2017-11-15 is offset from the pointing centre by $\sim$1.3 arcsec, that is, by $\sim$2 synthesized beamwidths due to proper motion effects described in Section 4.1. The position of the wide T3 brown dwarf companion at a separation $\sim$16.4 arcsec is marked by the square box. The cross indicates the correlation centre (pointing centre). (b) Stokes V image of 2M0213 AB. The binary is unresolved and enclosed in the circle with a red outline. The data has been phase-shifted to the true coordinates at epoch 2017-11-15. The binary is detected at a peak flux density of ~ -174 μJy beam^{-1} where the negative indicates the left circular polarization. The 1σ rms noise in the image is $\sim$4.6 μJy beam^{-1}. The source is detected at SNR $\sim$ 38. Similarly, the position of the wide T3 brown dwarf companion is marked by the square box. (c) Stokes I image of 2M0213 AB synthesized from e-MERLIN follow-up observations of the binary. The M4.5 component is detected and enclosed in the large circle. We do not show the position of the T3 dwarf since it is detected in the VLA data at a similar noise level to the e-MERLIN data at $\sim$16 μJy beam^{-1}. The synthesized beam in all images is indicated by the circle to the bottom left.

2017-11-15 which introduced an offset in the position of the system. For 2M0213 AB, we used the Gaia DR2 position (Lindegren et al. 2018) and proper motions from Best et al. (2020) to obtain the true position of the binary at the time of observation. We compared the propagated position (02h13m19.8952 + 36d48m51.6699s) to positions extracted from the image (02h13m20.68396s \+ 36d48m51.69034s) corresponding to an offset of $\sim$31 mas. The binary 2M0213 AB presented in Fig. 1(a) was detected at a peak flux density 356 $\pm$ 6.1 μJy beam^{-1} at a signal-to-noise ratio (SNR) $\sim$ 36. The flux density and position were obtained by fitting a Gaussian using CASA's `imfit` tool. Considering the offset is less than the imaging cell size ($\sim$140 mas) we confirm the detection of the M dwarf binary. The wide T3 component at 16.4 arcsec is not detected, although we have marked its position on the image using a square box. We have used the same astrometric parameters to propagate the coordinates to the e-MERLIN epoch 2025-02-15. We have detected a component at SNR $\sim$ 5 (see Fig. 1c). Using a similar Gaussian fit, we have determined a peak flux density 90.5 $\pm$ 7.5 μJy beam^{-1} at coordinates 02h13m20.70069s + 36d48m52.02129s (at observing dates 2025-03-13 to 2025-03-14). We find an offset of $\sim$12 mas in position between the pointing centre coordinates from *Gaia* propagated to epoch 2025. We note the M6.5 component is in orbit at $\sim$217 mas, which is $\sim$5 synthesized beamwidths from the pointing centre.

The L5 brown dwarf 2M0418 in the Hyades cluster is too faint to be detected by *Gaia*. The pointing centre for the observation used coordinates from the original processing of 2MASS at epoch 1997-10-31. Fortuitously, Lodieu et al. (2019) have, however, used the Liverpool telescope in the infrared to constrain the proper motions at $\mu_\alpha \approx 142.0 \pm 4.3$ mas yr^{-1}, $\mu_\delta \approx -51.8 \pm 4.0$ mas yr^{-1} and the parallax at 25.8 $\pm$ 2.9 mas. The position at epoch 2015.4 is also available from the CATWISE catalogue, which is a reprocessing of the Wide-field Infrared Survey Explorer (WISE) and NEOWISE catalogues (Marocco et al. 2021). Propagating the coordinates reveals the brown dwarf has shifted by $\sim$3 arcsec. We have not made a detection at the true position of 2M0418 indicated by a square box in Fig. 2. We however detect a radio source $\sim$5.″8 from the true position at $\sim 4\sigma$ and at a peak flux density of $\sim$16 μJy beam^{-1}. Using the source count flux density relationship $N(S) \simeq (23.2 \pm 2.8) S^{-1.18}$ arcmin^2 at 5 GHz (Fomalont 1989) which places the density of sources at $>$16 μJy beam^{-1} at $\sim 2.45 \times 10^{-4}$ arcsec^{-2}, the probability of the source being a false positive in an area $\sim$6 arcsec is $\sim 2.7 \times 10^{-2}$. Considering the large offset in position from the true position of 2M0418, the radio emission is unlikely to be the origin. However, it remains plausible that the emission is from a background AGN. There are no known associations between the source and existing radio catalogues.

4.2 Variability

To probe for variability, we first bin the visibilities at a two minute cadence as a compromise between sensitivity and temporal resolution and proceed to produce Stokes I and V light curves from the RR and LL correlations. We obtain the uncertainties by adding the thermal noise for a dual polarized robust weighted image ($\sigma_t \sim 16.7$ μJybeam^{-1}) observed over a cadence of two minutes[5] to a flux scaling error of $\sim$10% in quadrature. Flux scaling errors are associated with the flux scaling calibrators and occur due to challenges in determining the absolute flux density. The adopted flux scaling error is consistent with the recommendations provided by the VLA.[6] It should be noted that we include the flux scaling error for the Stokes I only as the Stokes V errors are uncharacterized. From the light curves generated from observations of 2M0213 AB presented in Fig. 3, we do not detect any statistically significant deviations at

[5] https://obs.vla.nrao.edu/ect/
[6] https://www.vla.nrao.edu/astro/calib/vlacal/cal_mon/last/1331 + 3030.html

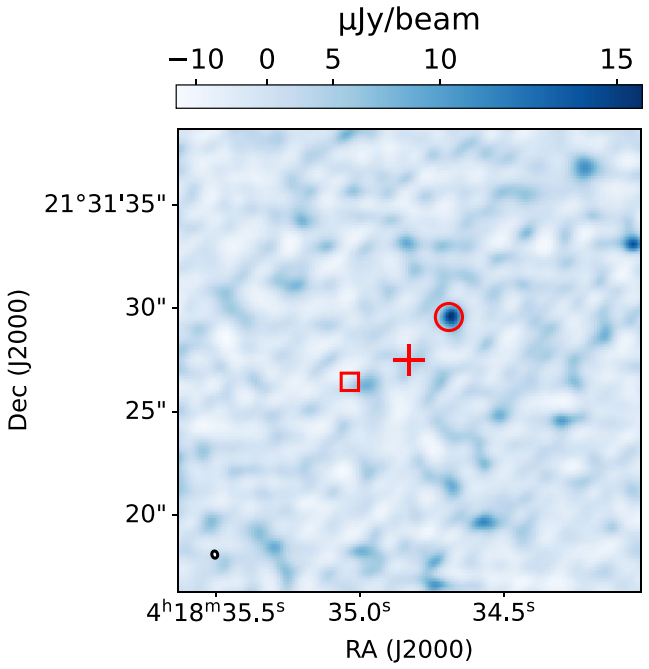

Figure 2. Stokes I image of 2M0418. The position of the L5 brown dwarf is marked by the square box in the image. A radio source was detected at 4σ, where σ is the thermal noise in the image, and at a peak flux density of $\sim$16 μJy beam^{-1},and is enclosed in the larger circle. The correlation centre (pointing centre) is indicated by the cross and the synthesized beam by the circle to the bottom left. We have not included Stokes V maps for observations of the L5 brown dwarf on account of the null detection.

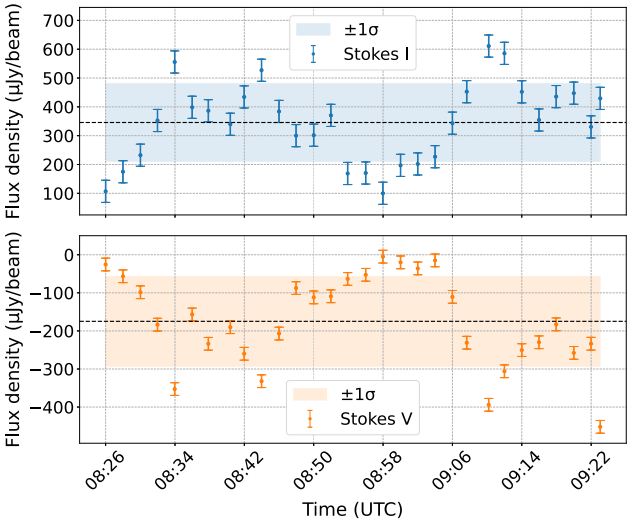

Figure 3. Flux light curves of 2M0213AB from the VLA data binned to a cadence of two minutes. The observation was ∼55 min long. The upper and lower subplots show the Stokes I and V light curves, respectively. The error bars represent the 1σ thermal noise added in quadrature to the flux scaling error and the shaded region represent a 1σ standard deviation of ∼133 μJybeam^{-1} and ∼118 μJybeam^{-1} in the Stokes I and V, respectively. The mean flux densities in the Stokes I and V are ∼347 μJybeam^{-1} and ~ -176 μJybeam^{-1}, respectively and are indicated by the dashed lines in the respective subplots. Note: These values slightly differ from values obtained using `imfit`.

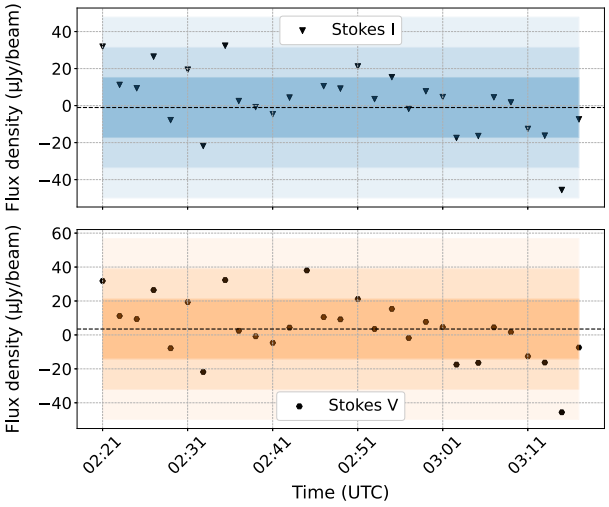

Figure 4. Flux light curves of 2M0418 from the VLA data binned to a cadence of two minutes. The observation was ∼55 min long. The upper and lower subplots show the Stokes I and V light curves, respectively. The shaded region indicate a 1, 2, and 3σ standard deviations from the mean flux density of ~ -1.0 μJybeam^{-1} and 3.5 μJybeam^{-1} for the Stokes I and V, respectively. The mean values are represented by the dashed lines. The 1σ standard deviation for the Stokes I and V is ∼16.3 μJybeam^{-1} and ∼17.8 μJybeam^{-1}, respectively which is consistent with the VLA's 1σ thermal noise estimated for a two minute cadence.

$>3\sigma$ from the mean indicating the source is in a quiescent state. Following the non-detection of 2M0418, we make a light curve binned at the same cadence as the 2M0213 AB light curve and estimate the uncertainties at a $3\sigma_t$ level. No pulses are detected as the flux densities are consistent with noise at a $3\sigma_t$ level. We present the Stokes I and V light curve of 2M0418 in Fig. 4.

4.3 The spectral energy distribution (SED) of the binary

For the SED fitting, we used PySSED (McDonald et al. 2024), a PYTHON tool for quick SED fitting. This tool collected optical photometry from the Panoramic Survey Telescope & Rapid Response System Data Release 1 (Pan-STARRS; Chambers et al. 2016) in the *grizy* filters, the American Association of Variable Star Observers's Photometric All-Sky Survey (APASS; Henden & Munari 2014) using the Johnson V and Sloan Digital Sky Survey (SDSS) gri filters, *Gaia* (Riello et al. 2021; Gaia Collaboration 2023) B_P, G, R_P filters, the Carlsberg Meridian Catalogue 15 (Muiños & Evans 2014) using SDSS r filter, 2MASS (Cutri et al. 2003) using the $VJHK$ filters, the WISE (Wright et al. 2010) in the mid-infrared at bandpasses of 3.4, 4.6, 12, and 22 μm and the reprocessed versions of WISE, catWISE (Marocco et al. 2021) and unWISE (Lang 2014). The BT-SETTL AGSS2009 atmosphere models (Allard, Homeier & Freytag 2011) have been used to generate model atmospheres. PySSED's default fitting parameters were used. The fit returns an effective temperature $T_{\rm eff} \sim 3016$ K and a stellar radius of $R_\star \sim 0.25\,R_\odot$. These values are characteristic of a mid-M dwarf and are consistent with the values for a M4 V dwarf derived by Pecaut & Mamajek (2013) with $T_{\rm eff} \sim 3200$ K. We note that the binary is unresolved in these catalogues. We have included the VLA measured flux densities at the edges of the lower and upper end of the observing band i.e. 4 and 8 GHz and are shown in the SED fit in Fig. 5. We have further extrapolated the fit to 8 GHz by fitting a simple power law under the assumption that the fluxes follow the trend of a concomitant

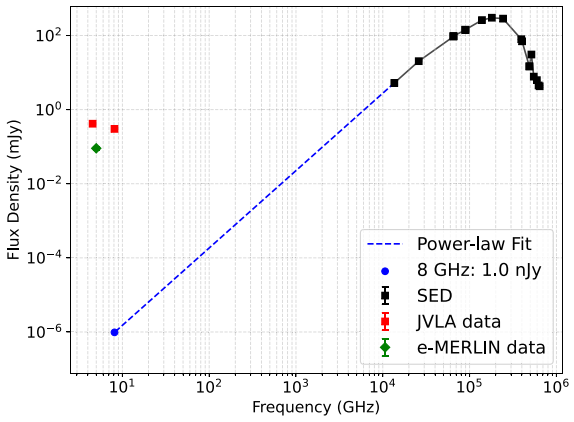

Figure 5. An SED fit of the unresolved binary. The solid curve represents the SED fit using different photometric catalogues described in Section 4.3, with each data point representing a different catalogue. Flux error bars are included for each data point, although they are not visible due to the scaling. The two square data points depict VLA fluxes at 4 and 8 GHz, respectively and the single diamond data point depicts e-MERLIN flux at 5 GHz. The broken line linking the SED data points to the data point at 8 GHz is a power law fit, which represents the expected flux for an SED extrapolated to 8 GHz.

decrease of the flux density with decreasing frequency. We note that although this idea is basic and a break in the power law is expected, it illustrates that the radio emission, which has flux densities $\sim 10^5$ larger than predicted by the power law, is generated by a very powerful mechanism presumably powered by magnetic activity.

4.4 Nature of the radio emission

To characterize the nature of the radio emission, we first measure the spectral index and the circular polarization fraction using the VLA data due to it's wide observing bandwidth, estimate brightness temperatures and luminosities, discuss the discrepancy in the flux densities measured using the VLA and e-MERLIN, and finally constrain the emission mechanism.

4.4.1 Spectral index and polarization

Following the procedure for measuring the spectral index described in Section 3.3, we determine an almost flat spectral index ($S \propto \nu^{\alpha}$) at $\alpha = -0.44 \pm 0.07$. We estimate the circular polarization fraction f_c by imaging the VLA data in the Stokes I and V (see Figs 1a and b) and evaluating the ratio $f_c = |V|/I$. The measured flux densities in Stokes I and V are $356 \pm 6.1\,\mu\mathrm{Jy\,beam^{-1}}$ and $-179.2 \pm 3.0\,\mu\mathrm{Jy\,beam^{-1}}$, respectively. Using the flux densities, we determine $f_c = 50.3 \pm 1.2\%$ and a mean $f_c = 45.20 \pm 1.58\%$ with the data binned to a two minute cadence.

4.4.2 Brightness temperature and luminosity

We determine the brightness temperature, T_B of the emission using the following relation (see Dulk 1985; Burgasser & Putman 2005)

$$T_B \simeq \frac{S_\nu}{1\,\mathrm{mJy}} \times \left(\frac{\nu}{1\,\mathrm{GHz}}\right)^{-2} \times \left(\frac{d}{1\,\mathrm{pc}}\right)^{2} \times \left(\frac{L}{1\,\mathrm{cm}}\right)^{-2} \times 10^{29}\ \ \mathrm{K}\,, \quad (1)$$

Table 2. Summary of results from the analysis.

Parameter	Value
Spectral index	-0.44 ± 0.07
Brightness temperature, T_B	$<10^{11}$ K
Bolometric luminosity, $\log_{10} L_{bol}$	31.25 erg s^{-1}
Radio luminosity, $\log_{10} L_R$	23.54 erg s^{-1}
Mean circular polarization fraction, f_c	$45.20 \pm 1.58\%$

where S_ν is the flux density in mJy, ν is the frequency in GHz, d is the distance to the binary in parsecs and L is the length of the emitting region in cm. We highlight that although we have made detections using the VLA and e-MERLIN data, useful brightness temperatures cannot be extracted from the images due to their low resolutions (1 arcsec at 6 GHz in the VLA's B configuration and 50 mas at 5 GHz for e-MERLIN). Following Berger (2002) and Phan-Bao et al. (2007), we assume $L \sim 0.1$ to $1 R_\star$ where $R_\star$ is the radius of the M4.5 primary. By adopting this approach and restricting the emission to a small region, we use equation (1) assess whether the brightness temperatures are in excess of the upper limit for incoherent emission from stellar corona at $\sim 10^{10}$ K (Dulk 1985). We determine $T_B \sim 6.6 \times 10^{10}$ K for $L \sim 0.1 R_\star$ and $T_B \sim 6.6 \times 10^{8}$ K for $L \sim 1 R_\star$. We highlight that our brightness temperature estimates neglect the source's morphology.

To determine the electron energies, we begin the analysis by assuming the source is optically thin ($\tau_\nu \ll 1$) and isolated and has a brightness temperature T_B. The effective temperature of the electrons T_{eff} is then determined as $T_B = \tau_\nu\ T_{eff}$ and for an optically thick source $T_B = T_{eff}$ (Dulk 1985). The lower bound for T_{eff} must then be $T_{eff} \geq T_B$ which is also consistent with an optically thick source. Admittedly T_{eff} can be determined using the models of Dulk & Marsh (1982) although they are restricted in applicability and require knowledge of the magnetic field strength B.

Using the brightness temperatures, we estimate electron energies, $E \sim 56.52$ keV–5.65 MeV for $T_{eff} \sim 6.6 \times 10^8$–$6.6 \times 10^{10}$ K. The effective temperature in the MeV results from the small length-scale used. Finally, we determine a bolometric luminosity $\log_{10} L_{bol} \sim 31.25$ erg s^{-1}, a spectral luminosity ($L_\nu = 4\pi S_\nu d^2$) of $\log L_\nu \sim 13.94$ erg s^{-1}Hz^{-1} and a radio luminosity ($L_R \approx L_\nu \Delta\nu$) of $\log_{10} L_R \sim 23.54$ erg s^{-1}. L_{bol} is determined from the Stefan Boltzmann's law using the effective temperature obtained from the SED fitting. The radio luminosity to the bolometric luminosity is $\log_{10} L_R / \log_{10} L_{bol} \sim -7.76$. We note that the luminosities determined from the VLA observations are upper limits. A summary of the values obtained from the analysis is presented in Table 2.

4.4.3 VLA and e-MERLIN flux discrepancy

The measured flux density using the VLA at $\sim 356\,\mu\mathrm{Jybeam^{-1}}$ is ~ 4 times greater than the corresponding e-MERLIN flux density. This difference may arise from a combination of factors, two of which are examined in detail here. The first factor to consider is the intrinsic variability of the binary. M dwarfs have been observed to exhibit long term magnetic cycles, for example, Ibañez Bustos et al. (2025) have recently measured cycling periods ranging from 3 to 19 yrs using 13 stars of spectral types ranging M0 to M6. Proxima Centauri, the mid-to-late M dwarf of spectral type M5.5 has a measured cyclic activity occurring at a period ranging from ~ 442 d (Cincunegui, Díaz & Mauas 2007) to 7–8 years (Wargelin et al. 2017, 2024) and brightens in the X-rays by a factor of ~ 1.5 at stellar maximum (Wargelin et al. 2024). Conversely, short term

variability is routinely observed in M dwarfs e.g. observations of Proxima Centauri between 1.1 and 3.1 GHz have detected intra-day variability attributed to flaring activity. The variability peaks at flux densities of 25 and 45 mJy which exceeds the average flux density by factors of 100 and 200, respectively (see Pérez-Torres et al. 2021). Consequently, considering the VLA observations are separated from the e-MERLIN observations by $\sim$ 8 years and the finding that mid-to-late M-dwarfs display short term variability, we cannot rule out intrinsic variability as a contributing factor to the flux difference.

Secondly, the VLA and e-MERLIN probe different scales owing to the the baseline lengths; the VLA in its B configuration has a maximum baseline of 11 km and e-MERLIN 217 km resulting in different synthesized beam ($\theta_{\rm synth}$) sizes. B configuration VLA observations at 6 GHz result in $\theta_{\rm synth} \sim 1$ arcsec and e-MERLIN observations at 5 GHz result in $\theta_{\rm synth} \sim 40$ mas. Accordingly, for the binary at a distance $\sim$14.28 pc, different linear spaces are probed. The VLA probes a linear scale of $\sim$14.28 au while the e-MERLIN probes a linear scale of $\sim$0.57 au. Therefore spatial filtering due to the disparate synthesized beam sizes cannot be dismissed as the higher resolution e-MERLIN could resolve out large scale emission that is otherwise well sampled by the low resolution VLA. Assuming a stellar radii, $R_\star \sim 0.25\,{\rm R}_\odot$ (see Section 4.3 for the justification), the spatial scale probed by e-MERLIN is of size $\sim 490\ R_\star$. Similarly to Climent et al. (2022), we find such a source size improbable, which seemingly implies the detected radio emission should originates from both components. However, this interpretation conflicts with the separation distance of $\sim$0.217 arcsec (3.1 au; Janson et al. 2014). Although the two components are within the synthesized beam of the VLA, they are separated by $\sim$5 beamwidths in the e-MERLIN observation. With an orbital period of 6.13–7.15 yrs (Janson et al. 2014), the binary separation distance is unlikely to significantly evolve over the time-scale of the VLA and e-MERLIN observing sessions to $\lesssim$40 mas. Consequently, we attribute the flux difference to variability. We recommend both higher resolution observations of the system and continued monitoring to characterize the variability.

4.4.4 *Emission mechanism*

A plausible radiation mechanism for the underlying spectral characteristics is mildly relativistic electrons radiating gyrosynchrotron emission. Following the spectral turnover at $\alpha = 0$, the emission is largely characterized by an optically thin spectral index and is produced by mildly relativistic electrons following a power law distribution $n(E) \propto E^{-\delta}$ where δ is the power law index. In this regime the emission exhibits a spectral index $\alpha = 1.22 - 0.9\delta$ (see Dulk & Marsh 1982) and a spectral power $\nu^{5/2}$ in the optically thick case (see Güdel 2002). Güdel (2002) have demonstrated that $2 \lesssim \delta \lesssim 4$ in stellar corona. We determine $\delta \sim 1.84$ which is consistent with their findings. The mean circular polarization fraction is on the high end of gyrosynchrotron emission. However, Golay et al. (2023) demonstrated that a gyrosynchrotron emission, which occurs at harmonics between 10 and 100 times the electron gyrofrequency, from a uniform magnetic field at optical depths $\ll$1 exhibits fractional polarization ratios ranging from $|V|/I \sim 90\%$ at lower harmonics to 10% at higher harmonics. We highlight that the flux densities from the Stokes V image are negative indicating the left circular polarization is dominant (see Fig. 1). In such a case, the emission is polarized in the sense of the ordinary (O)-mode suggesting optically thick gyrosynchrotron emission (see Dulk, Melrose & White 1979) seemingly presenting a contradiction with the interpretation of the spectral index. We note high polarization fractions are not uncharacteristic of optically thin gyrosynchrotron emission with pitch angle distributions. In such a scenario, the polarization mode is dependent on the viewing angle and the shape of the distribution (see Fleishman & Melnikov 2003).

To estimate the magnetic field strength B, the length of the emitting region L and the electron number density $n_{\rm e}$ we apply the semi-empirical solutions of the radiative transfer equation for gyrosynchrotron radiation from a non-thermal distribution of electrons by Dulk (1985) and Güdel (2002). We assume a viewing angle $\theta \sim \pi/3$ and $\delta = 3$ which is typical for stellar corona and similarly to Berger (2006), we determine the peak frequency $\nu_{\rm p}$ as

$$\nu_{\rm p} \approx 16.6 \times n_{\rm e}^{0.23} L^{0.23} \times B^{0.77} \times 10^3 \ \ {\rm Hz}, \tag{2}$$

the flux density as

$$S_{\nu,{\rm p}} \approx 1.54 \times B^{-0.76} \times L^2 \times d^{-2} \times \nu_{\rm p}^{2.76} \times 10^{-4} \ \ \mu{\rm Jy}, \tag{3}$$

and the fractional polarization ratio as

$$f_{\rm c} \approx 2.85 \times B^{0.51} \times \nu_{\rm p}^{-0.51} \times 10^3 \ \ . \tag{4}$$

Using $f_{\rm c} \sim 50.3\%$ which is estimated from the image plane and assuming the emission peaks at a frequency (at which the plasma transitions from optically thick to optically thick) $\nu_{\rm p} \lesssim 4$ GHz, we estimate $B < 174.86$ G, $L < 1.54 R_\star$, and $n_{\rm e} < 2.91 \times 10^5$ cm^{-3}.

We cannot entirely dismiss coherent emission produced through the electron cyclotron maser emission mechanism (ECME) due to the brightness temperatures which are in excess of 10^{10} for $L = 0.1 R_\star$. For ECME, the radio emission is at a local cyclotron $\nu_{\rm c} = 2.8 \times 10^{-3}\ B$ GHz which constrains the stellar magnetic field strength $B \sim 1.4$–2.8 kG.

Based on the spectral index, circular polarization fractions, which, although high, do not reach 100% fractional polarization typical of ECME (Hallinan et al. 2008), the calculated luminosities which are consistent to the same order of magnitude with luminosities for quiescent emission from M dwarfs (e.g. Burgasser & Putman 2005), lower bounds of electron energies which are in the range 1$\sim$100 keV and brightness temperatures (assuming an emission region on the scale of the stellar disc) and the persistent emission, we argue the emission is consistent with gyrosynchrotron radiation.

5 CONCLUSIONS

We have detected 2M0213 AB, a binary M dwarf system at a peak flux density of $\sim$356 μJy beam^{-1} using the VLA. By employing various astrometric catalogues, we have conclusively determined that the detected source corresponds to the binary. The radio emission from the binary is polarized at a mean circular polarization fraction $f_{\rm c} = 45.2 \pm 1.58\%$ and exhibits a spectral index $\alpha = -0.44 \pm 0.07$. We have used photometric SED fitting to constrain the radius of the M4.5 component to 0.25 M$_\odot$ and the effective temperature to 3016 K. The radio luminosity of the M dwarf binary is $\log L_{\rm R}/\log L_{\rm bol} \approx -7.76$. We have made follow-up observations of the binary using the e-MERLIN and detected a single component. From our higher angular resolution detection, we argue the emission at 5 GHz is potentially associated with the M4.5 primary, which may also display short or long term variability. Using Stokes I and V light curves, we have searched for short-term variability over the duration of the VLA observation and failed to detect any emission at $>3\sigma$ from the mean indicating the emission is quiescent. Continued monitoring of the binary using very long baseline interferometry should conclusively determine the active component and constrain the true variability.

Based on the electron energies, the brightness temperatures, radio luminosities and the spectral index, we have demonstrated the emission is consistent with gyrosynchrotron radiation. It is noteworthy that this detection adds to the already rare catalogue of binaries that have been probed for radio emission. Kao & Pineda (2025) have recently shown that binarity in UCDs increases the occurrence of radiation belts which are a prevailing explanation for the origin of quiescent emission in UCDs (see Leto et al. 2021; Climent et al. 2022). As such continued monitoring of binary systems not only adds to the sparse catalogue of radio active M dwarfs but may also determine the origin of the emissions.

Regrettably, we did not detect 2M0418. We detected a background AGN at an angular distance of ∼5.8 arcsec from the position of 2M0418 and at a peak flux density ∼16 μJy beam^{-1}. We have produced a light curve for the undetected 2M0418, searched for short duration bursts and made no detection at a significant level $>3\sigma$ from the mean. We note that among UCDs, L dwarfs have the lowest radio activity as ∼5% exhibit flares (Route & Wolszczan 2016) and ∼10–13% display quiescent emission (Kao & Shkolnik 2024). We highlight that chromospheric activity becomes increasingly rare towards later L spectral types (Schmidt et al. 2015) with ∼9.3% of mid-to-late L dwarfs exhibiting chromospheric activity in the form of Hα emission (Pineda et al. 2016). As such, the non-detection of 2M0418 is unsurprising considering the low detection fractions for L dwarfs. 2M0418 nevertheless remains intriguing given its chromospheric activity which is rare in mid L dwarfs.

ACKNOWLEDGEMENTS

This project has been made possible in part by a grant from the SETI Institute. This work made use of ASTROPY:3, a community-developed core PYTHON package and an ecosystem of tools and resources for astronomy (Astropy Collaboration 2013, 2018, 2022). This work has made use of data from the European Space Agency (ESA) mission *Gaia* (https://www.cosmos.esa.int/gaia), processed by the *Gaia* Data Processing and Analysis Consortium (DPAC, https://www.cosmos.esa.int/web/gaia/dpac/consortium). Funding for the DPAC has been provided by national institutions, in particular, the institutions participating in the *Gaia* Multilateral Agreement. The National Radio Astronomy Observatory is a facility of the National Science Foundation operated under cooperative agreement by Associated Universities, Inc. This research has made use of the SIMBAD database, operated at CDS, Strasbourg, France. This research has made use of the VizieR catalogue access tool, CDS, Strasbourg, France. e-MERLIN is a National Facility operated by the University of Manchester at Jodrell Bank Observatory on behalf of STFC. This publication makes use of data products from the WISE, which is a joint project of the University of California, Los Angeles, and the Jet Propulsion Laboratory/California Institute of Technology, funded by the National Aeronautics and Space Administration. We thank the anonymous referee for useful suggestions that have significantly improved the manuscript.

DATA AVAILABILITY

Data underlying this article are publicly available in the NRAO Data Archive at https://data.nrao.edu/portal and can be accessed with project code 17B-169. The e-MERLIN data will be provided upon reasonable request.

REFERENCES

Allard F., Homeier D., Freytag B., 2011, in Johns-Krull C., Browning M. K., West A. A., eds, ASP Conf. Ser.Vol. 448, 16th Cambridge Workshop on Cool Stars, Stellar Systems, and the Sun. Astron. Soc. Pac., San Francisco, p. 91
Antonova A., Hallinan G., Doyle J. G., Yu S., Kuznetsov A., Metodieva Y., Golden A., Cruz K. L., 2013, A&A, 549, A131
Astropy Collaboration, 2013, A&A, 558, A33
Astropy Collaboration, 2018, AJ, 156, 123
Astropy Collaboration, 2022, APJ, 935, 167
Baraffe I., Chabrier G., 2018, A&A, 619, A177
Basri G., Marcy G. W., Graham J. R., 1996, ApJ, 458, 600
Belokurov V. et al., 2020, MNRAS, 496, 1922
Berger E., 2002, ApJ, 572, 503
Berger E., 2006, ApJ, 648, 629
Best W. M. J., Liu M. C., Magnier E. A., Dupuy T. J., 2020, AJ, 159, 257
Bowler B. P. et al., 2023, AJ, 165, 164
Briggs D. S., 1995, American Astronomical Society Meeting Abstracts. p. 112.02
Browning M. K., 2008, ApJ, 676, 1262
Burgasser A. J., Putman M. E., 2005, ApJ, 626, 486
Burrows A. et al., 1997, ApJ, 491, 856
CASA Team et al., 2022, PASP, 134, 114501
Castro-Ginard A. et al., 2024, A&A, 688, A1
Chabrier G., Baraffe I., Phillips M., Debras F., 2023, A&A, 671, A119
Chabrier G., Küker M., 2006, A&A, 446, 1027
Chambers K. C. et al., 2016, preprint (arXiv:1612.05560)
Cincunegui C., Díaz R. F., Mauas P. J. D., 2007, A&A, 461, 1107
Climent J. B. et al., 2022, A&A, 660, A65
Cushing M. C. et al., 2006, ApJ, 648, 614
Cutri R. M. et al., 2003, 2MASS All Sky Catalog of point sources. NASA/IPAC Infrared Science Archive
Czesla S., Schneider P. C., Schmitt J. H. M. M., 2008, A&A, 491, 851
Deacon N. R. et al., 2017, MNRAS, 467, 1126
Dobler W., Stix M., Brandenburg A., 2006, ApJ, 638, 336
Dulk G. A., 1985, ARA&A, 23, 169
Dulk G. A., Marsh K. A., 1982, ApJ, 259, 350
Dulk G. A., Melrose D. B., White S. M., 1979, ApJ, 234, 1137
Fleishman G. D., Melnikov V. F., 2003, ApJ, 587, 823
Fomalont E. B., 1989, in Perley R. A., Schwab F. R., Bridle A. H., eds, ASP Conf. Ser.Vol. 6, Synthesis Imaging in Radio Astronomy. Astron. Soc. Pac., San Francisco, p. 213
Gaia Collaboration, 2018, A&A, 616, A1
Gaia Collaboration, 2023, A&A, 674, A1
Gandhi P, Buckley D A H, Charles P A, Hodgkin S, Scaringi S, Knigge C, Rao A, Paice J A, Zhao Y, 2022, MNRAS, 510, 3885
Garrington S. T. et al., 2004, in Oschmann J. M., Jr, ed., Proc. SPIE Conf. Ser.Vol. 5489, Ground-based Telescopes. SPIE, Bellingham, p. 332
Golay W. W., Mutel R. L., Lipman D., Güdel M., 2023, MNRAS, 522, 1394
Golovin A., Reffert S., Just A., Jordan S., Vani A., Jahreiß H., 2023, A&A, 670, A19
Güdel M., 2002, ARA&A, 40, 217
Guedel M., Benz A. O., 1993, ApJ, 405, L63
Hallinan G., Antonova A., Doyle J. G., Bourke S., Lane C., Golden A., 2008, ApJ, 684, 644
Hawley S. L., Gizis J. E., Reid I. N., 1996, AJ, 112, 2799
Henden A., Munari U., 2014, Contrib. Astron. Observatory Skalnate Pleso, 43, 518
Henry T. J., Jao W.-C., Subasavage J. P., Beaulieu T. D., Ianna P. A., Costa E., Méndez R. A., 2006, AJ, 132, 2360
Ibañez Bustos R. V., Buccino A. P., Nardetto N., Mourard D., Flores M., Mauas P. J. D., 2025, A&A, 696, A230
Janson M. et al., 2012, ApJ, 754, 44
Janson M., Bergfors C., Brandner W., Kudryavtseva N., Hormuth F., Hippler S., Henning T., 2014, ApJ, 789, 102
Kao M. M., Pineda J. S., 2025, MNRAS, 539, 2292
Kao M. M., Shkolnik E. L., 2024, MNRAS, 527, 6835

Kent B. R. et al., 2020, in Pizzo R., Deul E. R., Mol J. D., de Plaa J., Verkouter H., eds, ASP Conf. Ser.Vol. 527, Astronomical Data Analysis Software and Systems XXIX. Astron. Soc. Pac., San Francisco, p. 571
Kirkpatrick J. D. et al., 1999, ApJ, 519, 802
Kumar S. S., 1962, AJ, 67, 579
Lang D., 2014, AJ, 147, 108
Lépine S., Gaidos E., 2011, AJ, 142, 138
Leto P. et al., 2021, MNRAS, 507, 1979
Lindegren L. et al., 2018, A&A, 616, A2
Lindegren L. et al., 2021, A&A, 649, A2
Lindegren L., Lammers U., Hobbs D., O'Mullane W., Bastian U., Hernández J., 2012, A&A, 538, A78
Lodieu N., Rebolo R., Pérez-Garrido A., 2018, A&A, 615, L12
Lodieu N., Smart R. L., Pérez-Garrido A., Silvotti R., 2019, A&A, 623, A35
Marocco F. et al., 2021, ApJS, 253, 8
McDonald I., Zijlstra A. A., Cox N. L. J., Alexander E. L., Csukai A., Ramkumar R., Hollings A., 2024, RAS Tech. Instrum., 3, 89
McLean M., Berger E., Reiners A., 2012. ApJ, 746, 23
Melrose D. B., 1980, Space Sci. Rev., 26, 3
Melrose D. B., 2017, Rev. Mod. Plasma Phys., 1, 5
Melrose D. B., Dulk G. A., 1982, ApJ, 259, 844
Mohanty S., Basri G., Shu F., Allard F., Chabrier G., 2002, ApJ, 571, 469
Moldon J., 2018, Proc. Sci., 14th European VLBI Network Symposium and Users Meeting (EVN 2018). SISSA, Trieste, PoS#152
Morgan D. P., West A. A., Garcés A., Catalán S., Dhital S., Fuchs M., Silvestri N. M., 2012, AJ, 144, 93
Muiños J. L., Evans D. W., 2014, Astron. Nachr., 335, 367
Nelson L. A., Rappaport S., Chiang E., 1993, ApJ, 413, 364
Newton E. R., Irwin J., Charbonneau D., Berlind P., Calkins M. L., Mink J., 2017, ApJ, 834, 85
Nindos A., 2020, Front. Astron. Space Sci., 7, 57
Parker E. N., 1955, ApJ, 122, 293
Pecaut M. J., Mamajek E. E., 2013, ApJS, 208, 9
Pérez-Garrido A., Lodieu N., Rebolo R., 2017, A&A, 599, A78
Pérez-Torres M. et al., 2021, A&A, 645, A77
Phan-Bao N., Osten R. A., Lim J., Martín E. L., Ho P. T. P., 2007, ApJ, 658, 553
Pineda J. S., Hallinan G., Kirkpatrick J. D., Cotter G., Kao M. M., Mooley K., 2016, ApJ, 826, 73
Rau U., Cornwell T. J., 2011, A&A, 532, A71
Rebolo R., Martin E. L., Basri G., Marcy G. W., Zapatero-Osorio M. R., 1996, ApJ, 469, L53
Reiners A., 2012, Living Rev. Sol. Phys., 9, 1
Reiners A., Homeier D., Hauschildt P. H., Allard F., 2007, A&A, 473, 245
Riaz B., Gizis J. E., Harvin J., 2006, AJ, 132, 866
Riello M. et al., 2021, A&A, 649, A3
Route M., Wolszczan A., 2016, ApJ, 830, 85
Schmidt S. J., Hawley S. L., West A. A., Bochanski J. J., Davenport J. R. A., Ge J., Schneider D. P., 2015, AJ, 149, 158
Skrutskie M. F. et al., 2006, AJ, 131, 1163
Stassun K. G. et al., 2011, in Johns-Krull C., Browning M. K., West A. A., eds, ASP Conf. Ser.Vol.448, 16th Cambridge Workshop on Cool Stars, Stellar Systems, and the Sun. Astron. Soc. Pac., San Francisco, p. 505
Vilhu O., 1984, A&A, 133, 117
Wargelin B. J., Saar S. H., Irving Z. A., Slavin J. D., Ratzlaff P., do Nascimento J.-D., 2024, ApJ, 977, 144
Wargelin B. J., Saar S. H., Pojmański G., Drake J. J., Kashyap V. L., 2017, MNRAS, 464, 3281
Winters J. G. et al., 2019, AJ, 157, 216
Wright E. L. et al., 2010, AJ, 140, 1868
Wu C. S., Lee L. C., 1979, ApJ, 230, 621

This paper has been typeset from a TEX/LATEX file prepared by the author.